Supplement of Clim. Past, 22, 1401–1421, 2026
https://doi.org/10.5194/cp-22-1401-2026-supplement
© Author(s) 2026. CC BY 4.0 License.

Supplement of

Holocene temperatures in southwestern Greenland controlled by topography, ice sheet proximity, and oceanic conditions

Sudip Acharya et al.

Correspondence to: Sudip Acharya (sudipach@buffalo.edu)

The copyright of individual parts of the supplement might differ from the article licence.

Supplementary Figures:

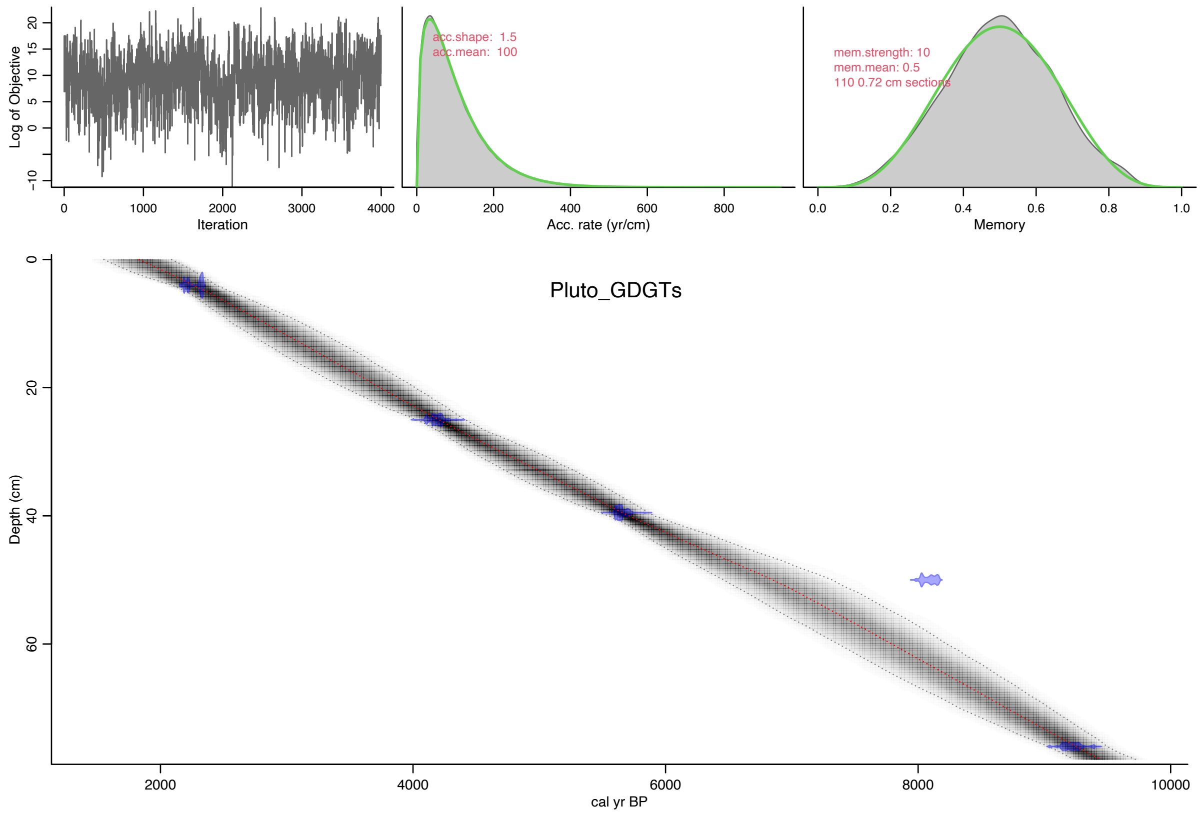

Figure S1: Age-depth model for the sediment core from Pluto lake. Age-depth model is based on five radiocarbon ages from aquatic macrofossils (Thomas et al., 2020), generated using rbacon in geochronR (Blaauw & Christen, 2011; McKay et al., 2021). Blue symbols indicate calibrated radiocarbon ages using IntCal20 (Reimer et al., 2020). Gray shading indicates the 95% confidence interval for the generated age-depth model.

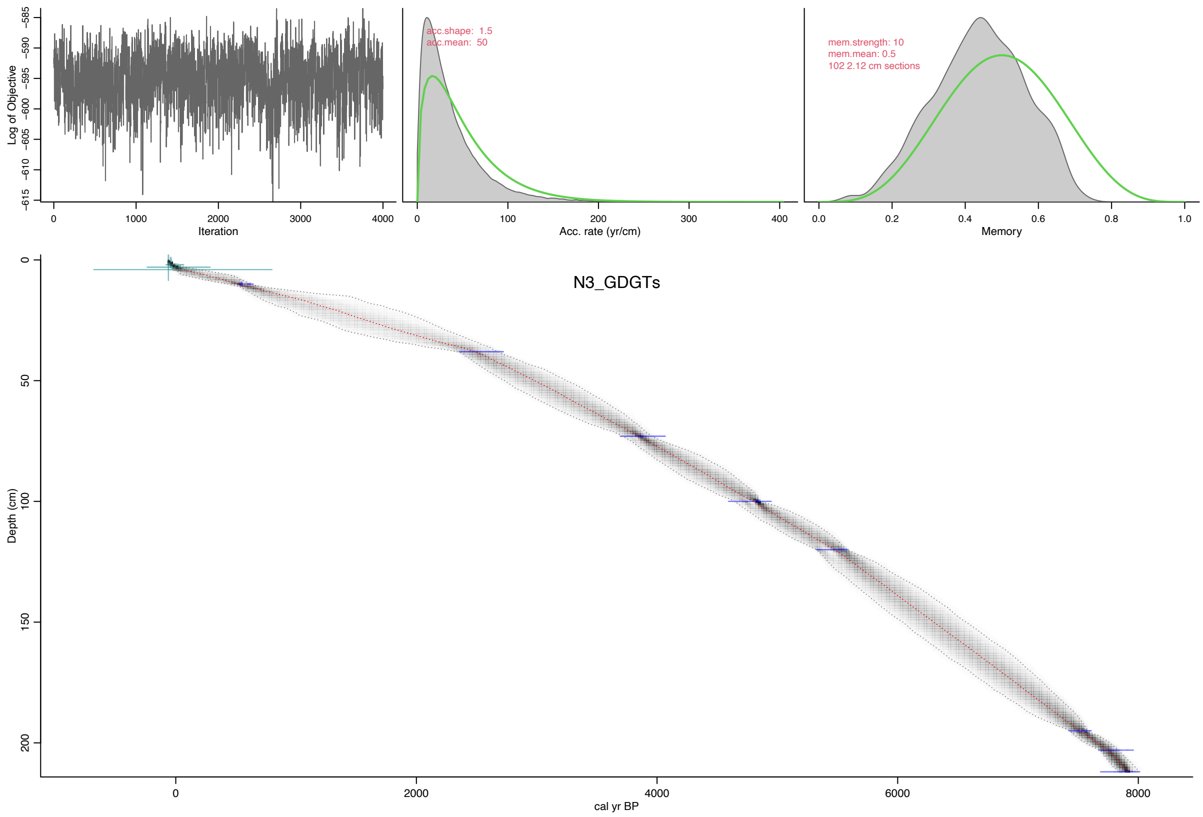

Figure S2: Age-depth model for the sediment core from N3 lake. Age-age-depth model is based on eight radiocarbon ages from aquatic macrofossils (blue symbols) and ^{210}Pb ages (green symbols) for the upper 4 cm (Thomas et al., 2016), generated using rbacon in geochronR (Blaauw & Christen, 2011; McKay et al., 2021). Blue symbols indicate calibrated radiocarbon ages using IntCal20 (Reimer et al., 2020). Green symbols indicate the ^{210}Pb ages. Gray shading indicates the 95% confidence interval for the generated age-depth model. Please refer to (Thomas et al., 2016) for detailed age-depth model description.

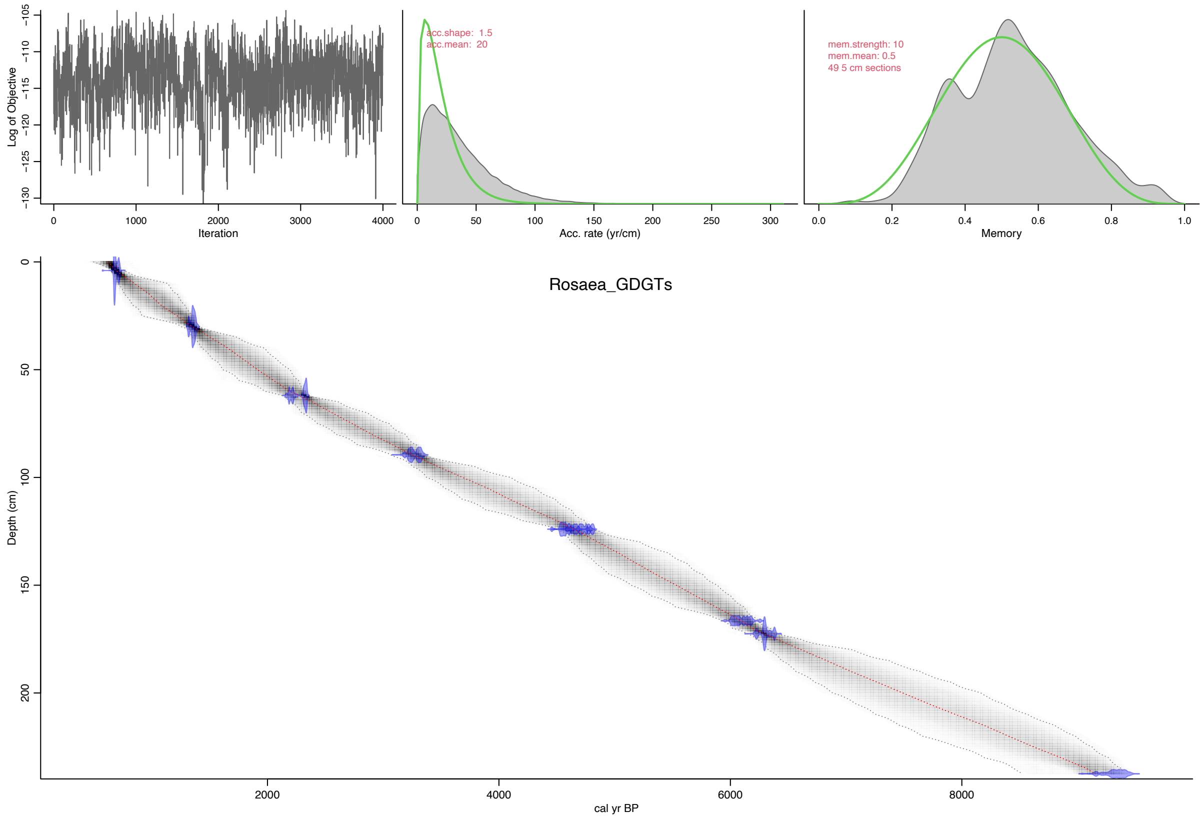

Figure S3: Age-depth model for the sediment core from Rosaea lake. Age-depth model is based on eight radiocarbon ages from aquatic macrofossils, generated using rbacon in geochronR (Blaauw & Christen, 2011; McKay et al., 2021). Blue symbols indicate calibrated radiocarbon ages using IntCal20 (Reimer et al., 2020). Gray shading indicates the 95% confidence interval for the generated age-depth model.

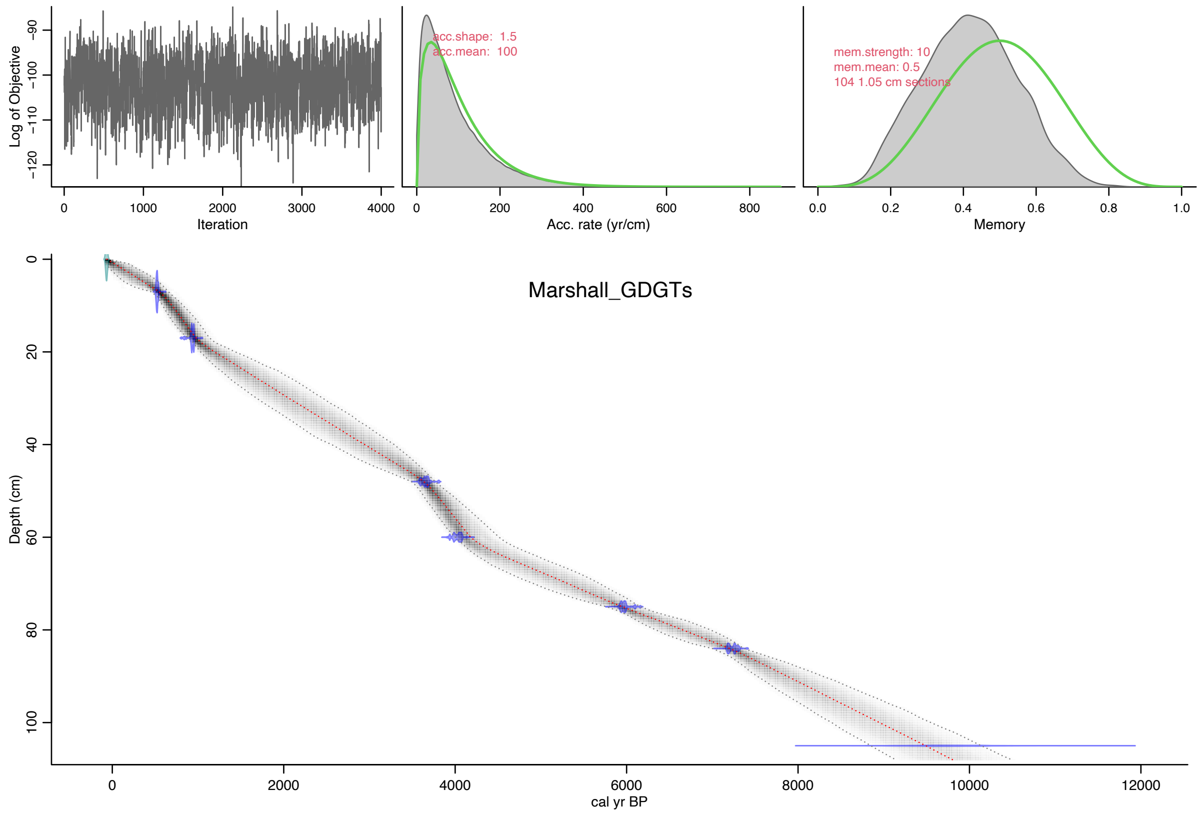

Figure S4: Age-depth model for the sediment core from Marshall lake. Age-depth model is based on seven radiocarbon ages from aquatic macrofossils, generated using rbacon in geochronR (Blaauw & Christen, 2011; McKay et al., 2021). Blue symbols indicate calibrated radiocarbon ages using IntCal20 (Reimer et al., 2020). Green symbol indicates an assumed calendar age of 2017 CE, because this core contained an intact sediment-water interface. Gray shading indicates the 95% confidence interval for the generated age-depth model.

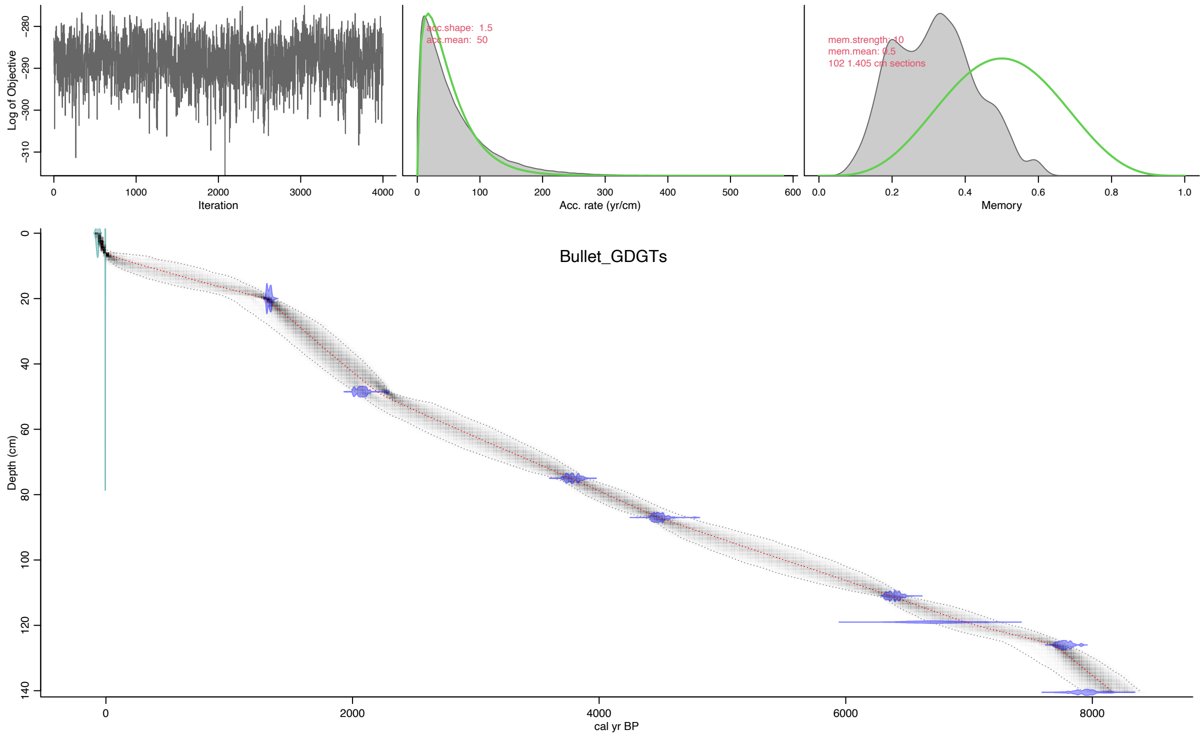

Figure S5: Age-depth model for the sediment core from Bullet lake. Age-depth model is based on eight radiocarbon ages from aquatic macrofossils, generated using R bacon in geochronR (Blaauw & Christen, 2011; McKay et al., 2021). Blue symbols indicate calibrated radiocarbon ages using IntCal20 (Reimer et al., 2020). Green symbol at 0 cm depth indicates the year of core collection and at 5 cm indicates the calibrated age using Northern Hemisphere Zone 1 compilation for post-bomb-age samples (Hua et al., 2013). Gray shading indicates the 95% confidence interval for the generated age-depth model.

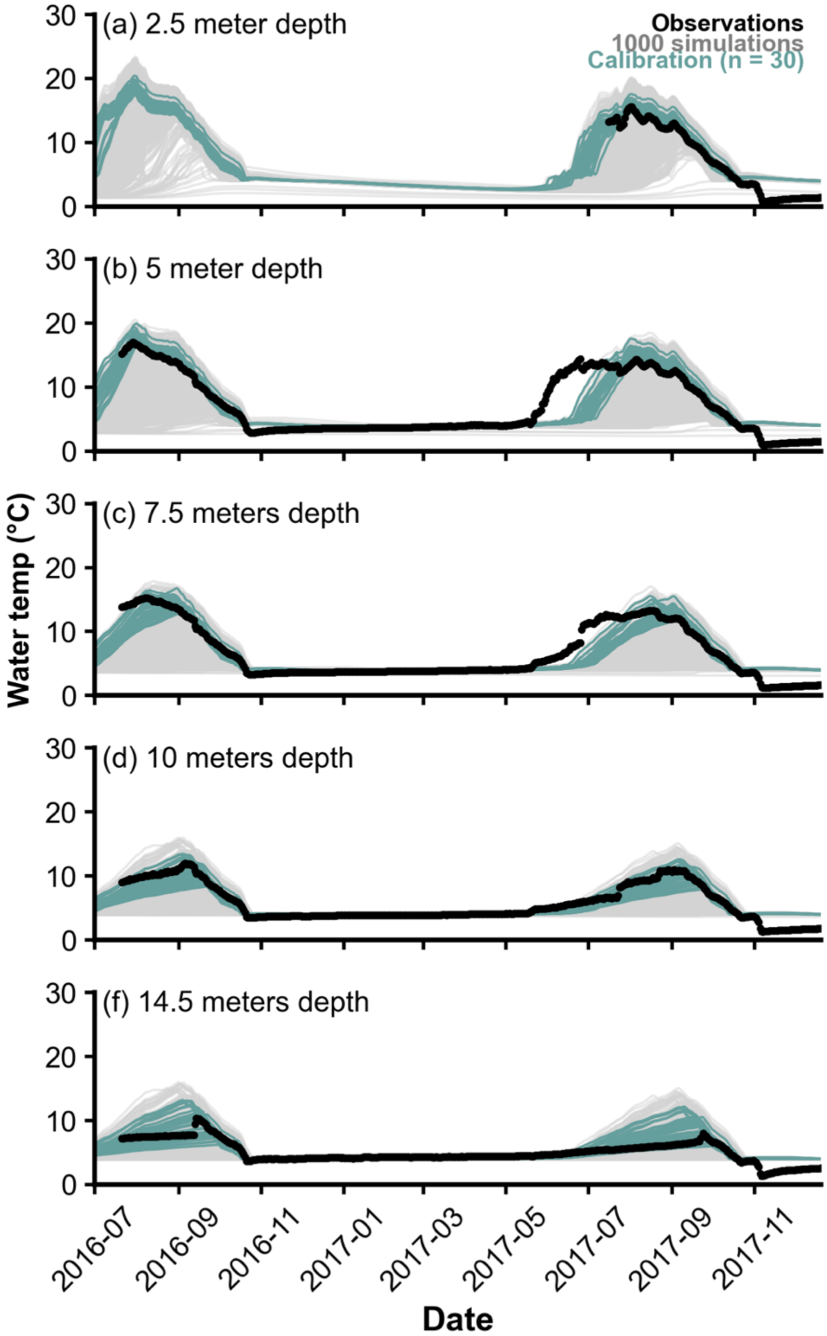

Figure S6: Lake model parameter calibration. Water temperatures at depths of 2.5, 5, 7.5, 10, and 14 meters in Lake 578, with black dots indicating observations; grey lines indicate simulations across the full range of uncertain thermodynamic balance parameters in 1000 ensembles; and the green line indicates simulations under parameters that most closely match observations.

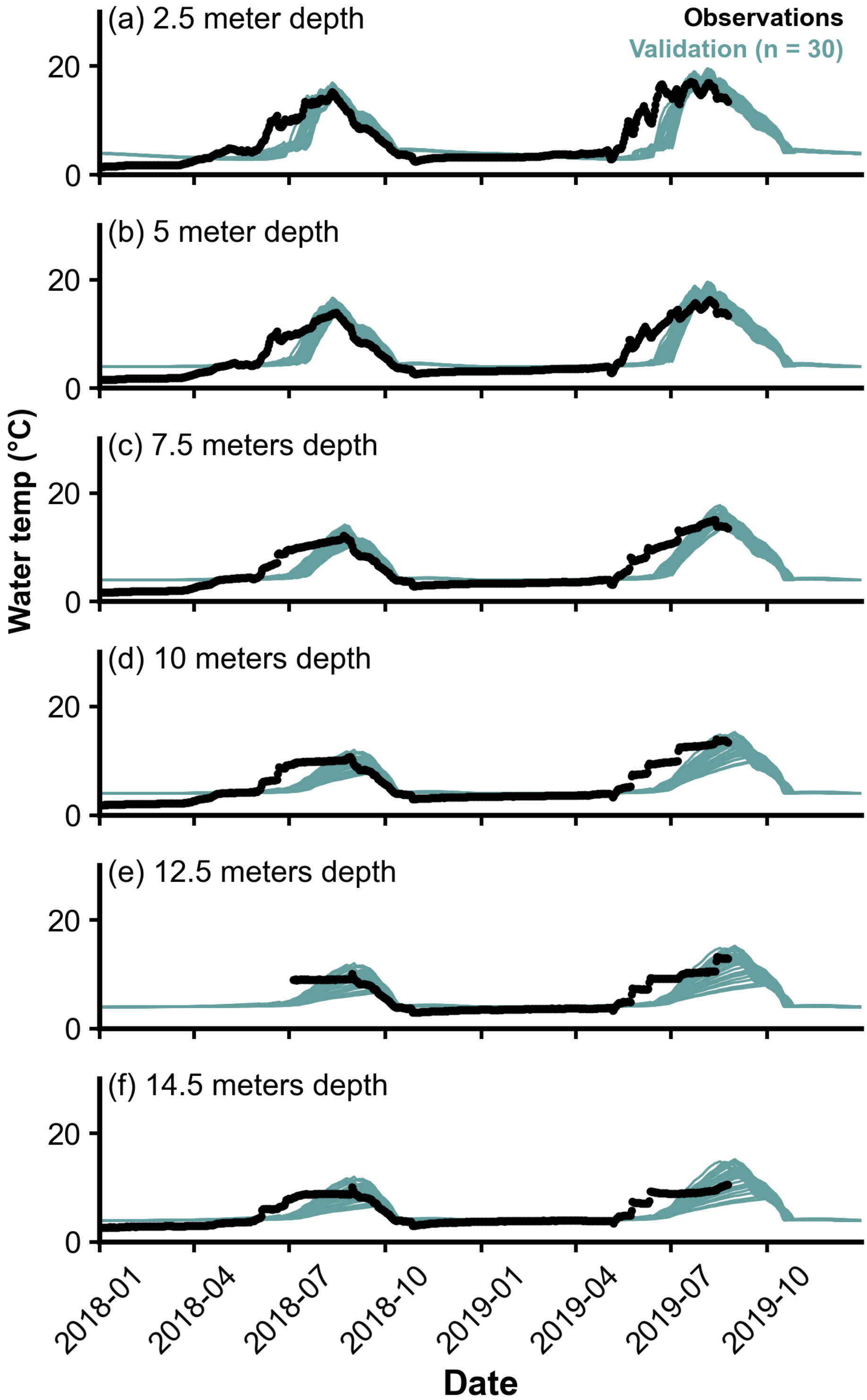

Figure S7. Lake model parameter validation. Comparison of water temperature at depths 2.5, 5, 7.5, 10, 12.5, and 14 m in Lake 578 between model outputs and observations, with black dots indicating observations and the green line indicating the simulations using ERA5 data and identified best-performing parameters (Zhao et al., 2021).

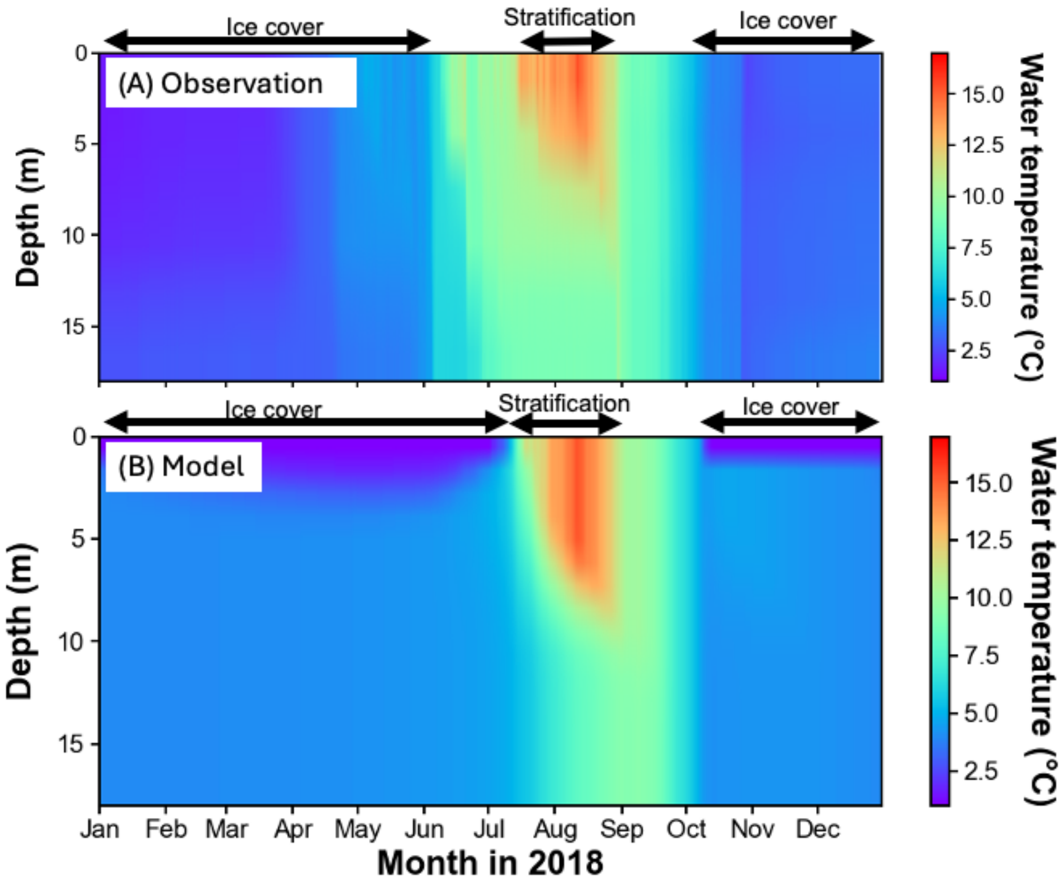

Figure S8: Comparison of thermal structure of Lake 578 based on (a) observations and (b) model simulations (Zhao et al., 2021) for 2018. The ice cover and stratification duration in the model simulations and observations are indicated by the arrows at the top of each plot. It should be noted that observation temperaure data for are only available at 2.5, 5, 7.5, 10, 12.5, and 14 m water depths, and are interpolated for other depths. The lake is isothermal during the periods between stratification and ice cover.

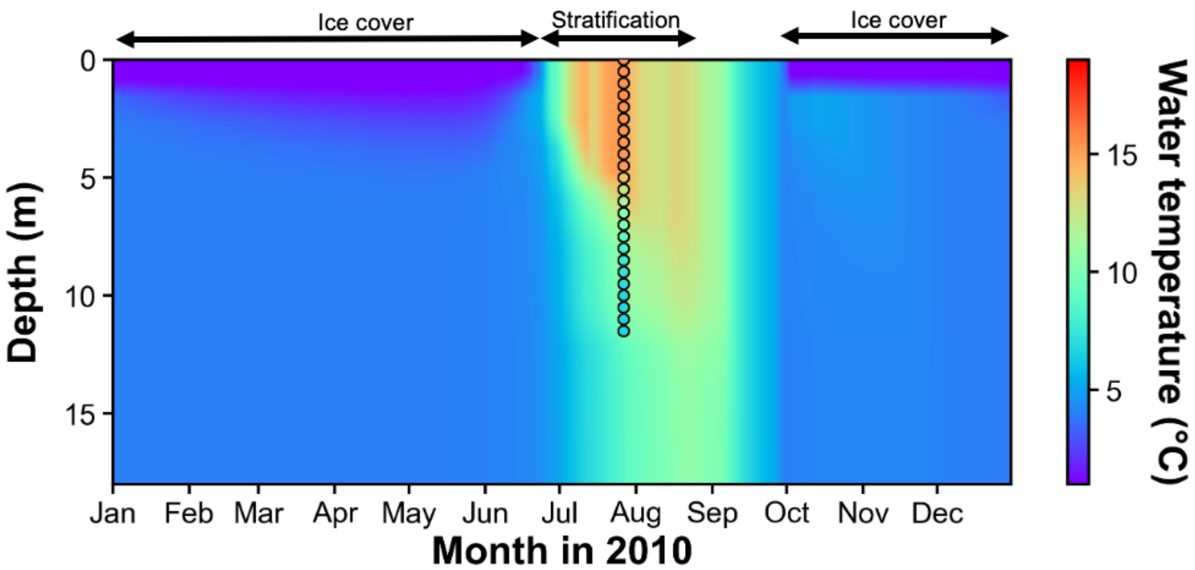

Figure S9: Comparison of thermal structure of Lake N3 based on model simulations and observations (indicated by circles) for 2010 (Corcoran et al., 2021). The ice cover and stratification duration in the model simulations are indicated by the arrows at the top of the plot. The lake is isothermal during the periods between stratification and ice cover.

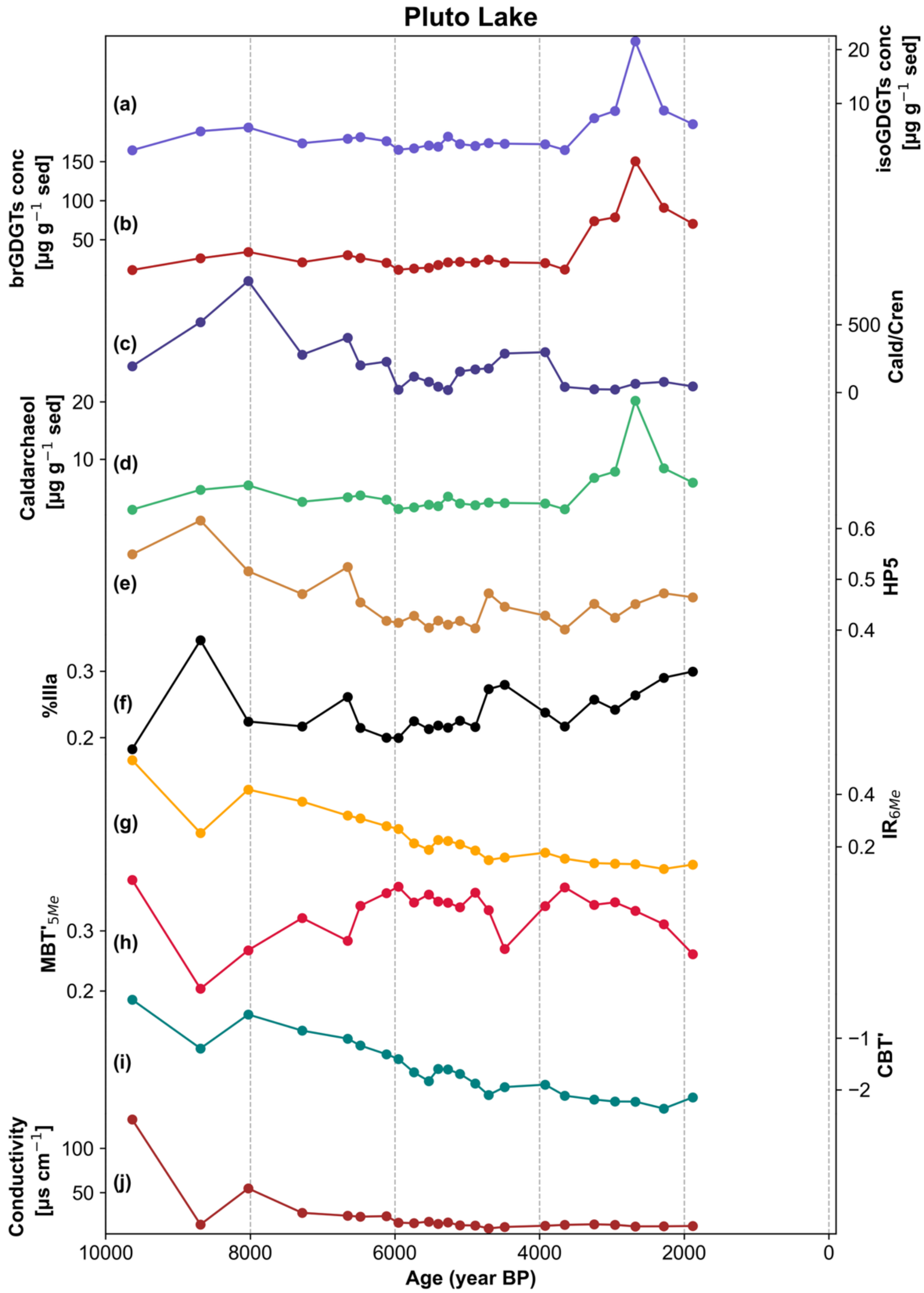

Figure S10: The downcore pattern of GDGTs and their indices in Lake Pluto sediments. (a) Isoprenoid (iso) GDGTs concentration in ng g^{-1} of dry sediment [ng g^{-1} sed], (b) branched (br) GDGTs concentration in ng g^{-1} of dry sediment [ng g^{-1} sed], (c) ratio of Caldarchaeol to Crenarchaeol (Cald/Cren), (d) concentration of Caldarchaeol in µg g^{-1} of dry sediment [µg g^{-1} sed], (e) ratio of the 5-methyl hexamethylated and pentamethylated brGDGTs with no cyclopentane rings (HP5), (f) fractional abundance of brGDGT IIIa (%IIIa), (g) isomerization ratio (IR_{6ME}), (h) methylation of branched tetraethers (MBT'_{5Me}), (i) cyclization of branched tetraethers (CBT′), and (j) inferred conductivity [µs cm^{-1}] (Raberg et al., 2021).

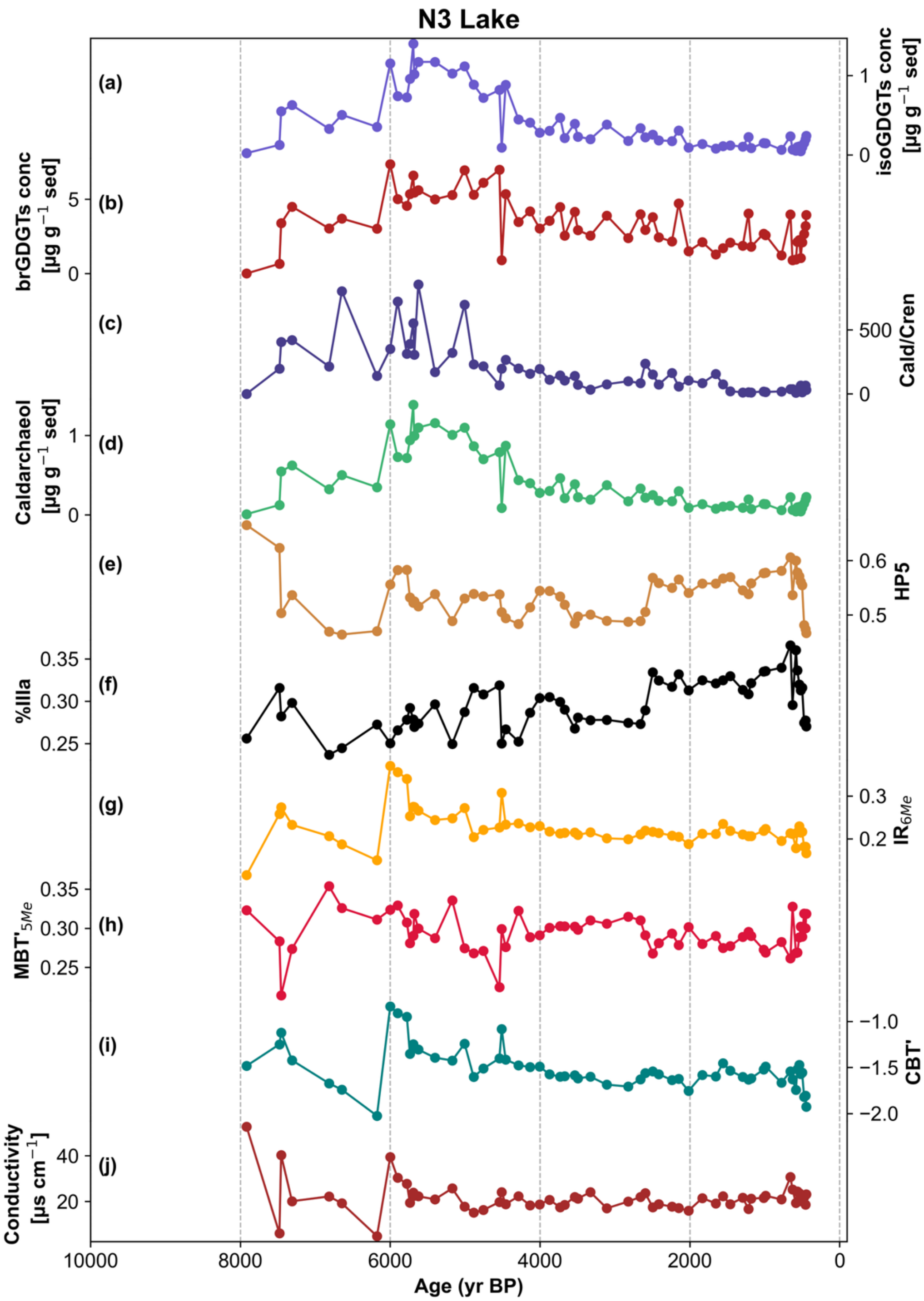

Figure S11: The downcore pattern of GDGTs and their indices in Lake N3 sediments. (a) Isoprenoid (iso) GDGTs concentration in ng g^{-1} of dry sediment [ng g^{-1} sed], (b) branched (br) GDGTs concentration in ng g^{-1} of dry sediment [ng g^{-1} sed], (c) ratio of Caldarchaeol to Crenarchaeol (Cald/Cren), (d) concentration of Caldarchaeol in μg g^{-1} of dry sediment [μg g^{-1} sed], (e) ratio of the 5-methyl hexamethylated and pentamethylated brGDGTs with no cyclopentane rings (HP5), (f) fractional abundance of brGDGT IIIa (%IIIa), (g) isomerization ratio (IR_{6ME}), (h) methylation of branched tetraethers (MBT'_{5Me}), (i) cyclization of branched tetraethers (CBT′), and (j) inferred conductivity [μs cm^{-1}] (Raberg et al., 2021).

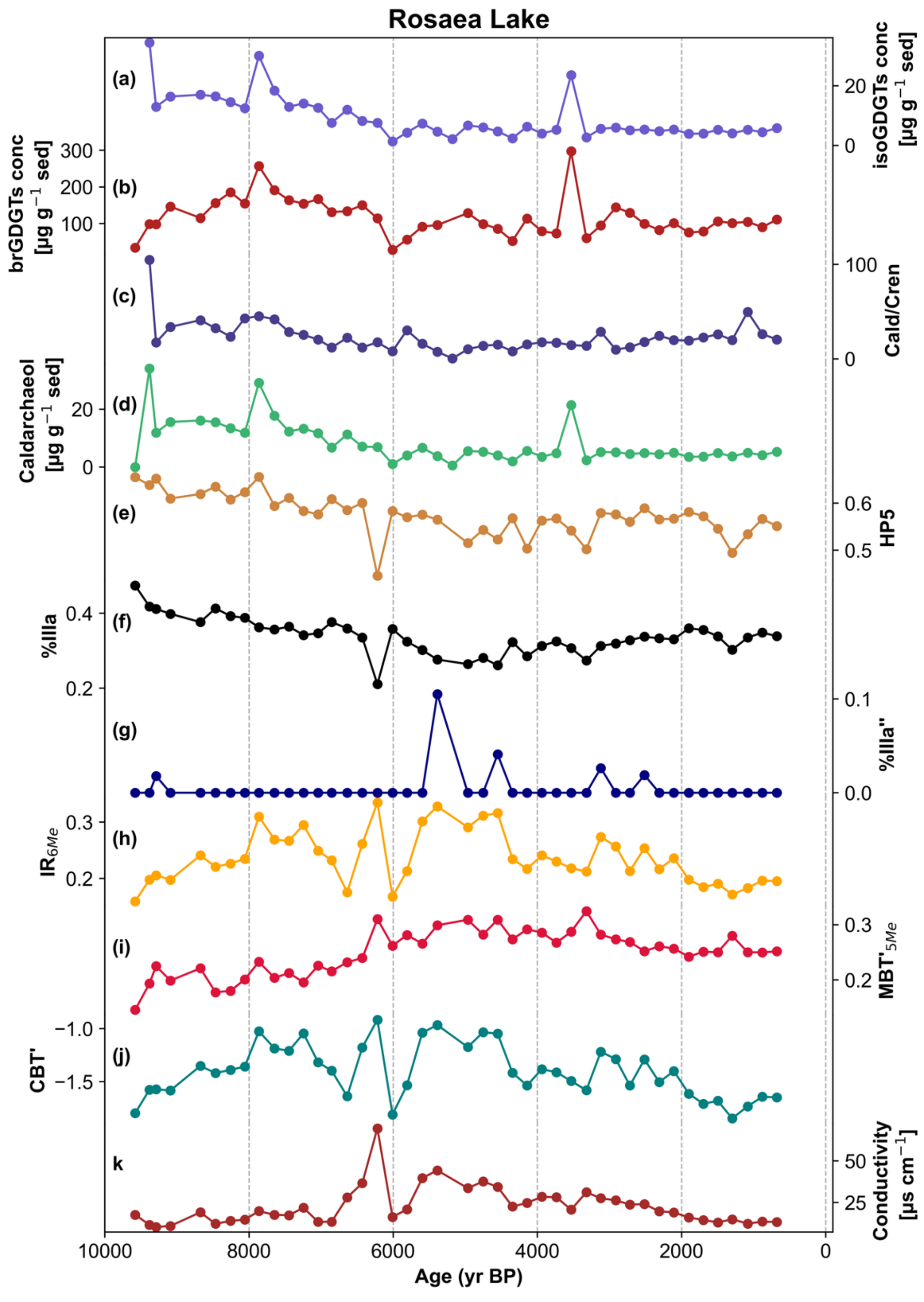

Figure S12: The downcore pattern of GDGTs and their indices in Lake Rosaea sediments. (a) Isoprenoid (iso) GDGTs concentration in ng g^{-1} of dry sediment [ng g^{-1} sed], (b) branched (br) GDGTs concentration in ng g^{-1} of dry sediment [ng g^{-1} sed], (c) ratio of Caldarchaeol to Crenarchaeol (Cald/Cren), (d) concentration of Caldarchaeol in µg g^{-1} of dry sediment [µg g^{-1} sed], (e) ratio of the 5-methyl hexamethylated and pentamethylated brGDGTs with no cyclopentane rings (HP5), (f) fractional abundance of brGDGT IIIa (%IIIa), (g) fractional abundance of brGDGT IIIa″ (Weber et al., 2015), (h) isomerization ratio (IR_{6ME}), (i) methylation of branched tetraethers (MBT'_{5Me}), (j) cyclization of branched tetraethers (CBT′), and (k) inferred conductivity [µs cm^{-1}] (Raberg et al., 2021).

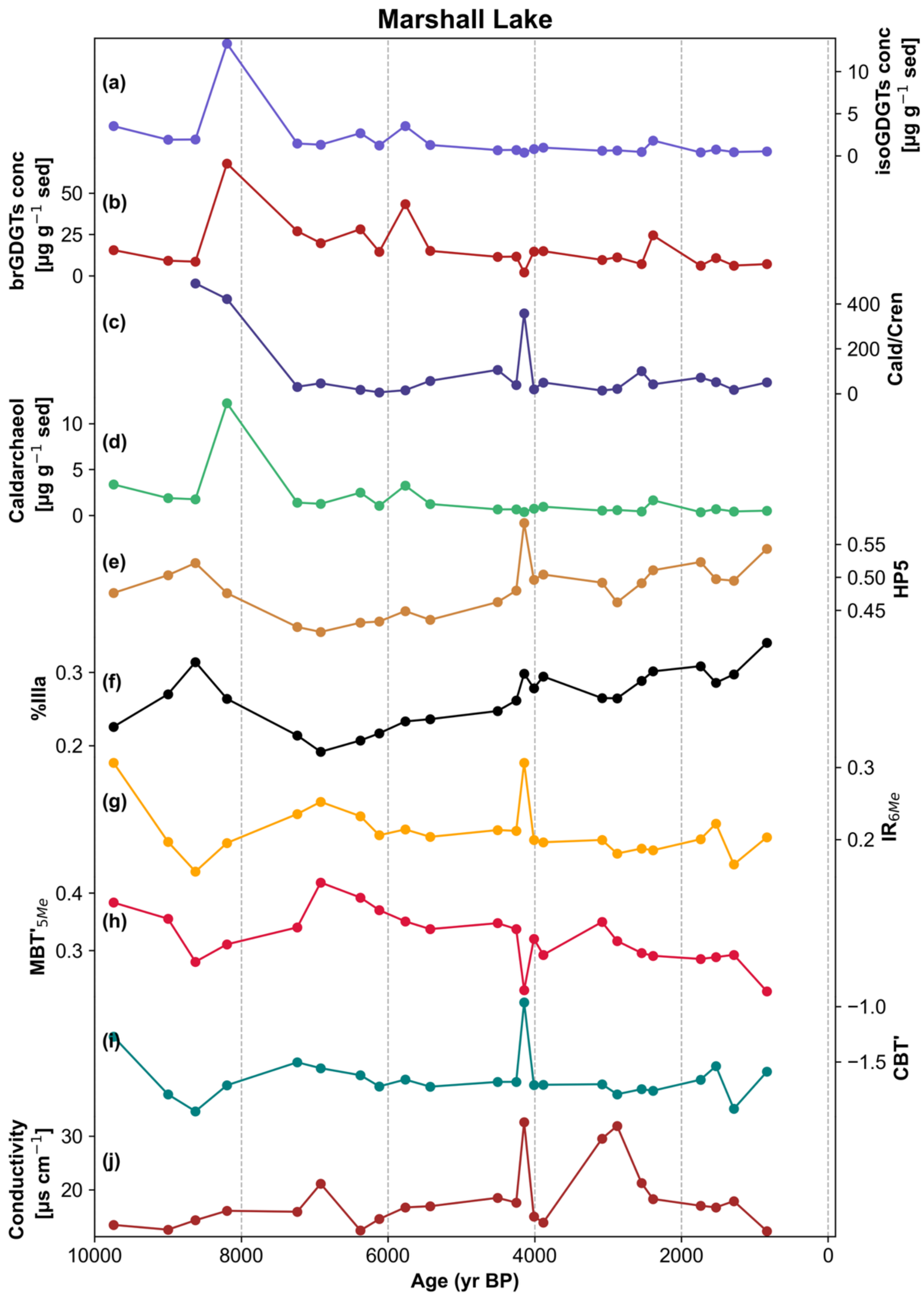

Figure S13: The downcore pattern of GDGTs and their indices in Lake Marshall sediments. (a) Isoprenoid (iso) GDGTs concentration in ng g^{-1} of dry sediment [ng g^{-1} sed], (b) branched (br) GDGTs concentration in ng g^{-1} of dry sediment [ng g^{-1} sed], (c) ratio of Caldarchaeol to Crenarchaeol (Cald/Cren), (d) concentration of Caldarchaeol in µg g^{-1} of dry sediment [µg g^{-1} sed], (e) ratio of the 5-methyl hexamethylated and pentamethylated brGDGTs with no cyclopentane rings (HP5), (f) fractional abundance of brGDGT IIIa (%IIIa), (g) isomerization ratio (IR_{6ME}), (h) methylation of branched tetraethers (MBT'_{5Me}), (i) cyclization of branched tetraethers (CBT′), and (j) inferred conductivity [µs cm^{-1}] (Raberg et al., 2021).

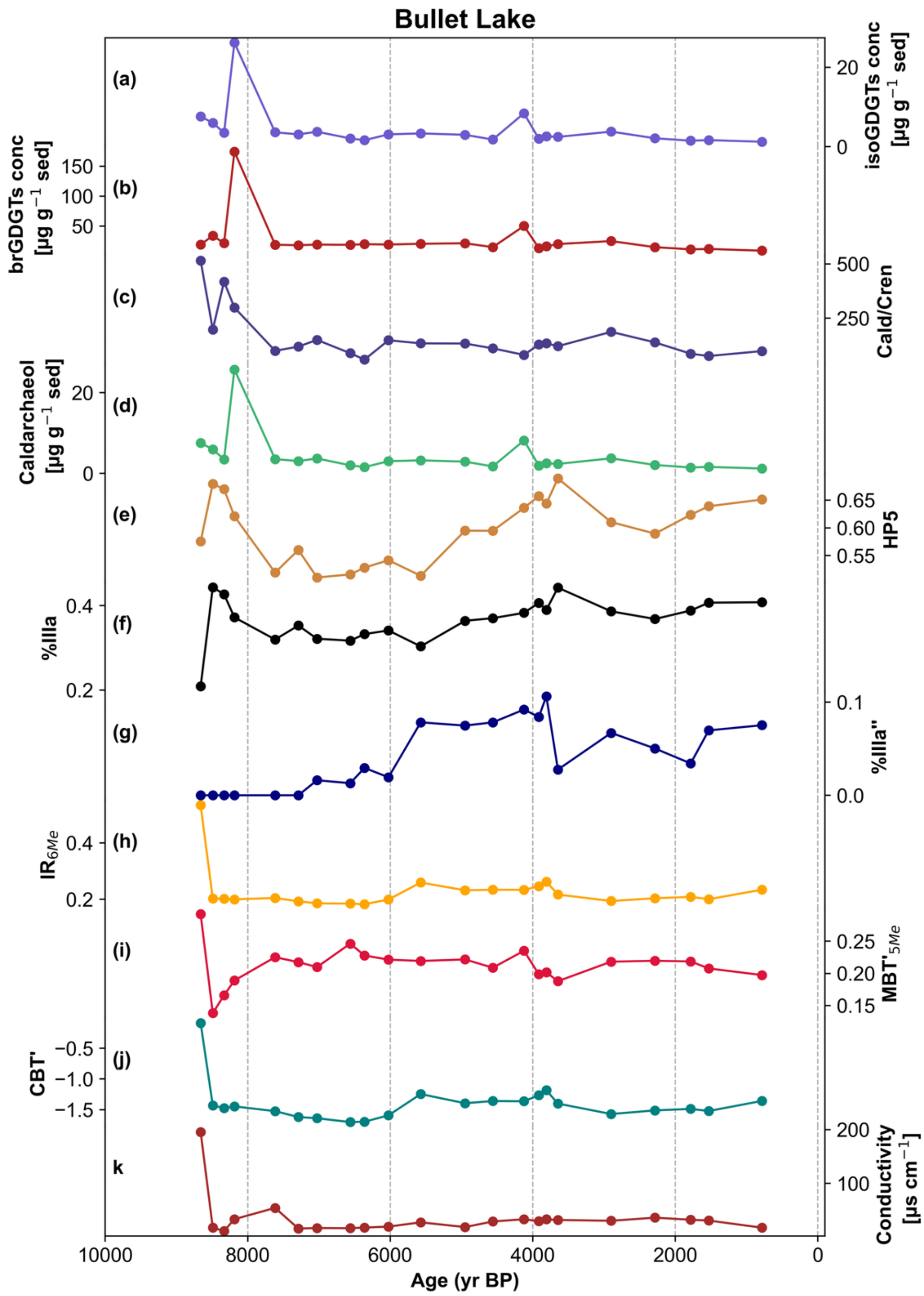

Figure S14: The downcore pattern of GDGTs and their indices in Lake Bullet sediments. (a) Isoprenoid (iso) GDGTs concentration in ng g^{-1} of dry sediment [ng g^{-1} sed], (b) branched (br) GDGTs concentration in ng g^{-1} of dry sediment [ng g^{-1} sed], (c) ratio of Caldarchaeol to Crenarchaeol (Cald/Cren), (d) concentration of Caldarchaeol in µg g^{-1} of dry sediment [µg g^{-1} sed], (e) ratio of the 5-methyl hexamethylated and pentamethylated brGDGTs with no cyclopentane rings (HP5), (f) fractional abundance of brGDGT IIIa (%IIIa), (g) fractional abundance of brGDGT IIIa″ (Weber et al., 2015), (h) isomerization ratio (IR$_{6ME}$), (i) methylation of branched tetraethers (MBT′$_{5Me}$), (j) cyclization of branched tetraethers (CBT′), and (k) inferred conductivity [µs cm^{-1}] (Raberg et al., 2021).

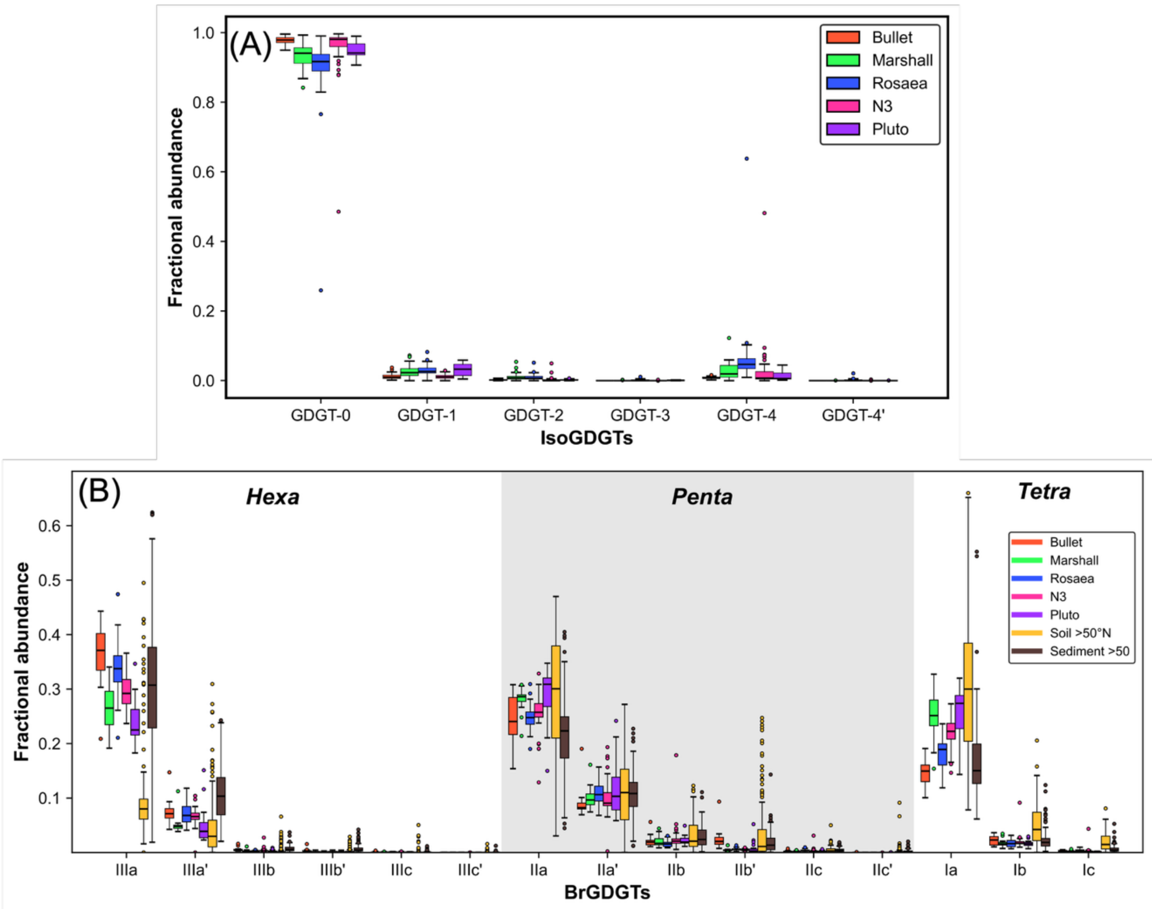

Figure S15: (a) Fractional abundance of isoGDGTs. (b) Comparison of fractional abundance of brGDGTs from southwestern Greenland lakes with high latitude (>50°N) soil and lake sediment samples.

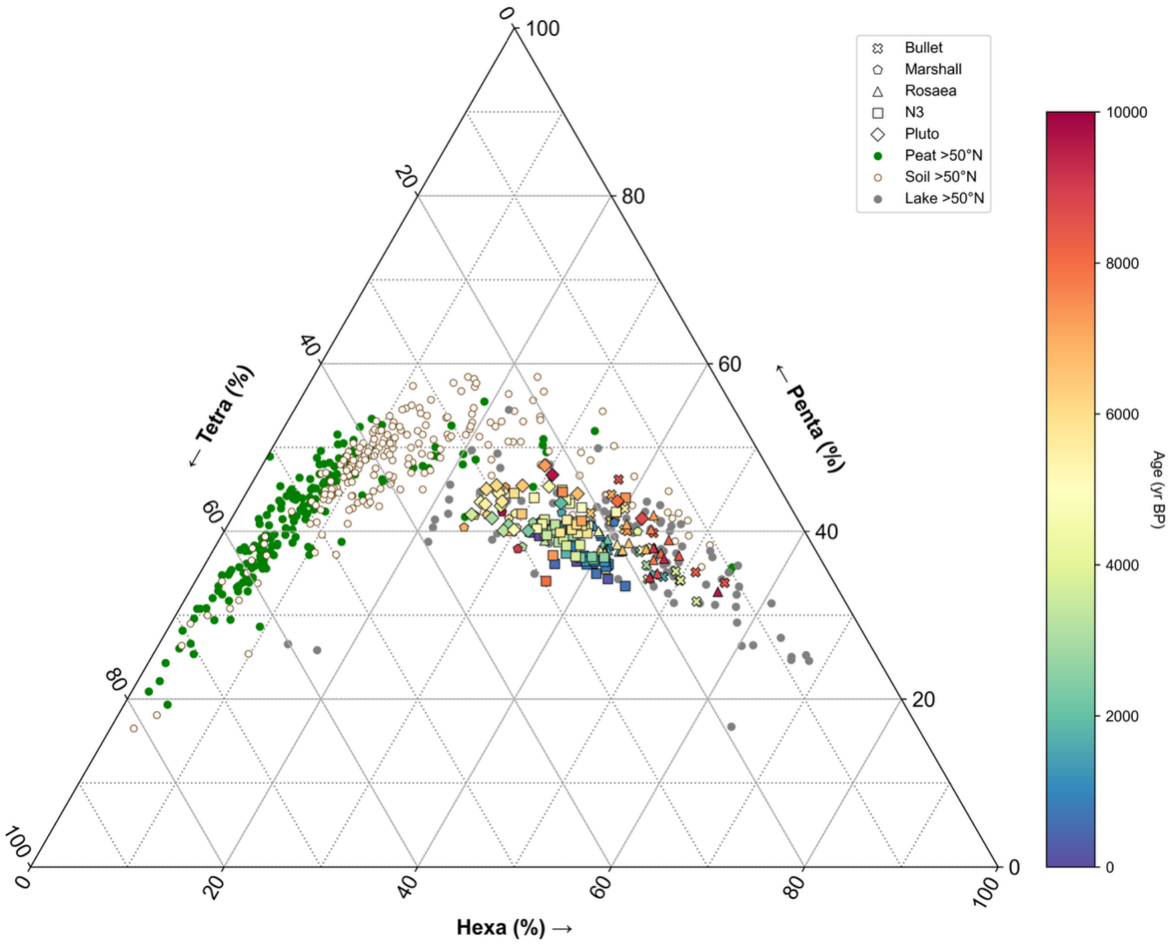

Figure S16: Ternary diagram showing the fractional abundance of hexa, penta and tetra methylated brGDGTs from southwestern Greenland lakes, compared to high latitude (>50°N) soil, lake sediment and peat samples.

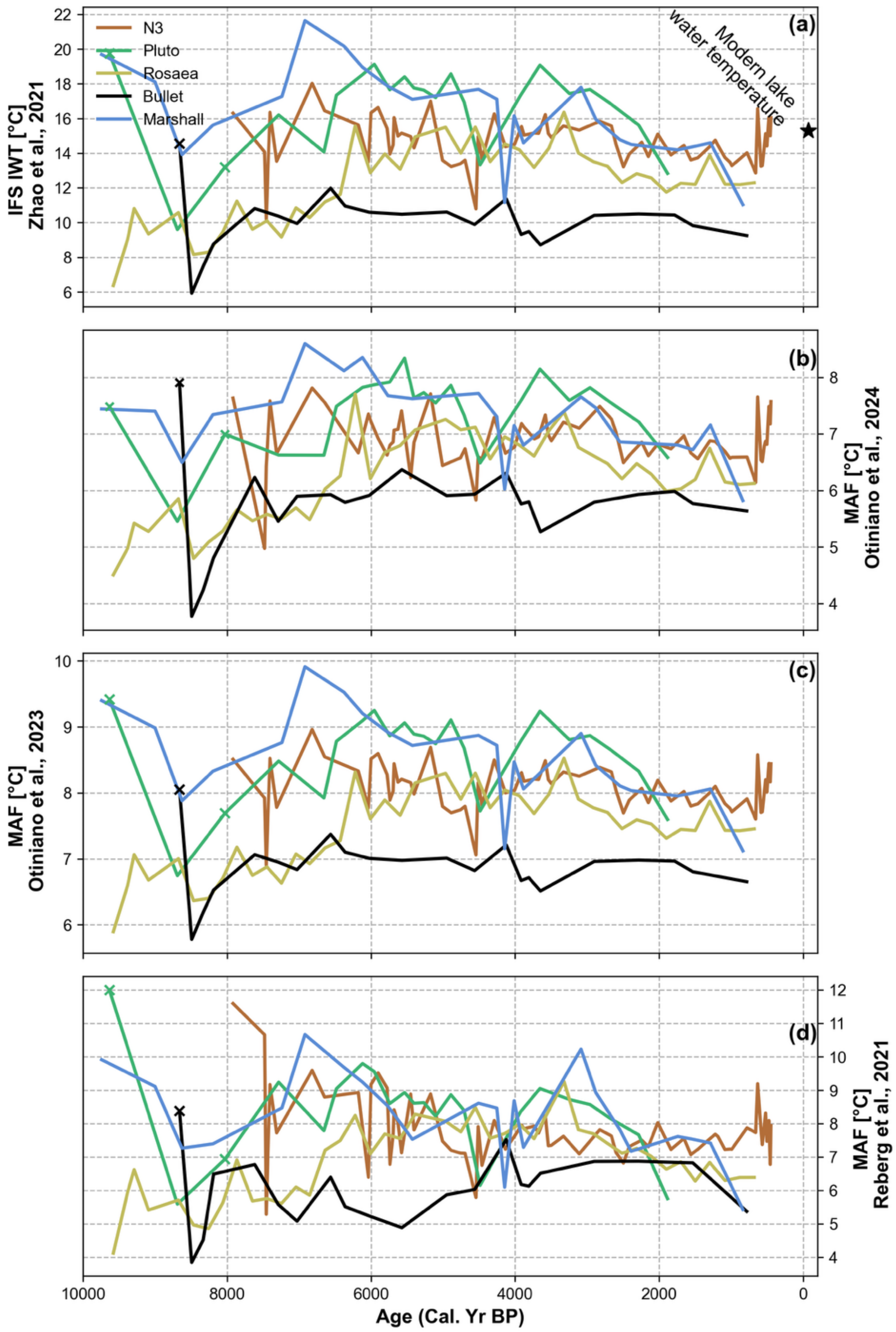

Figure S17: Reconstructed Holocene temperatures in southwestern Greenland lakes using (a) Zhao et al., (2021), (b) Otiniano et al., (2024), (c) Otiniano et al., (2023), and (d) Raberg et al., (2021) calibrations. Samples with IR_{6ME}>0.4, which are interpreted to be affected by non thermal effect on brGDGTs, are indicated by X. Black star symbol in (a) indicates the the moden July lake water temperature from N3 lake. ISF LWT represents ice free season lake water tempeature and MAF represents mean air temperate above freezing.

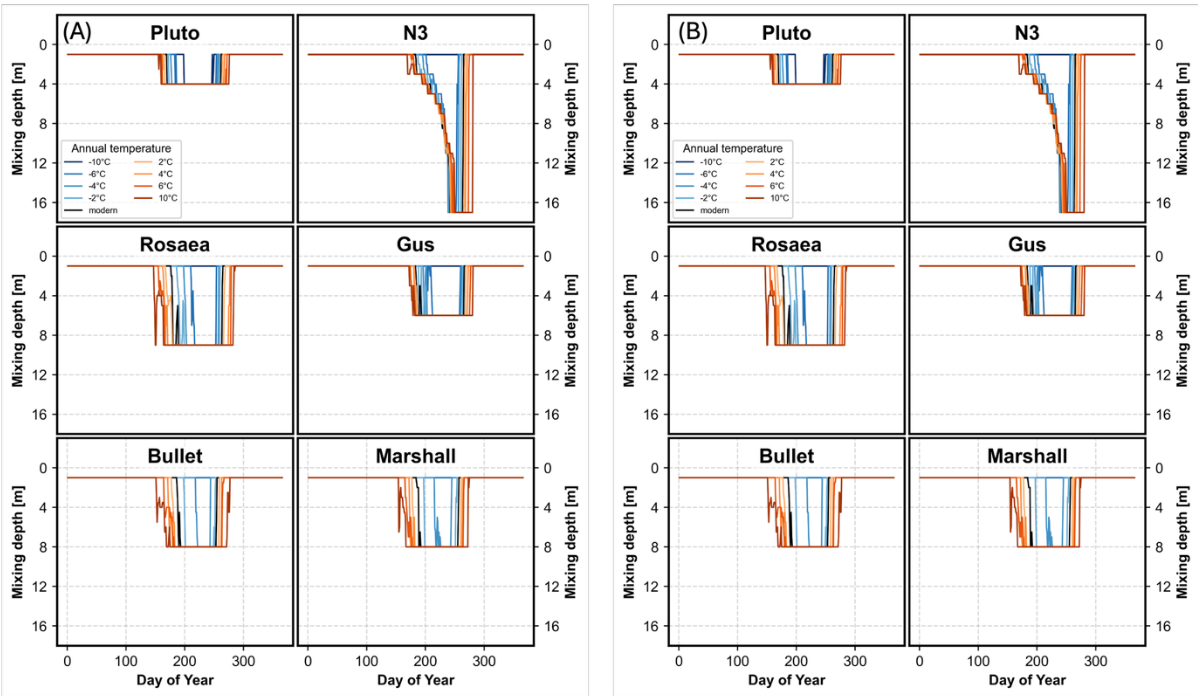

Figure S18: Simulated mixing depth [m] in study lakes with changes in (A) annual air temperature, and (B) JJAS air temperature. Modern represents the model run under the current ERA5 climate conditions. All model runs are plotted as the median over 30-year periods. The initial spring increase in mixing depth coincides with the onset of ice-free season in all simulations, and the fall decrease in mixing depth to 0 m coincides with the end of the ice-free season.

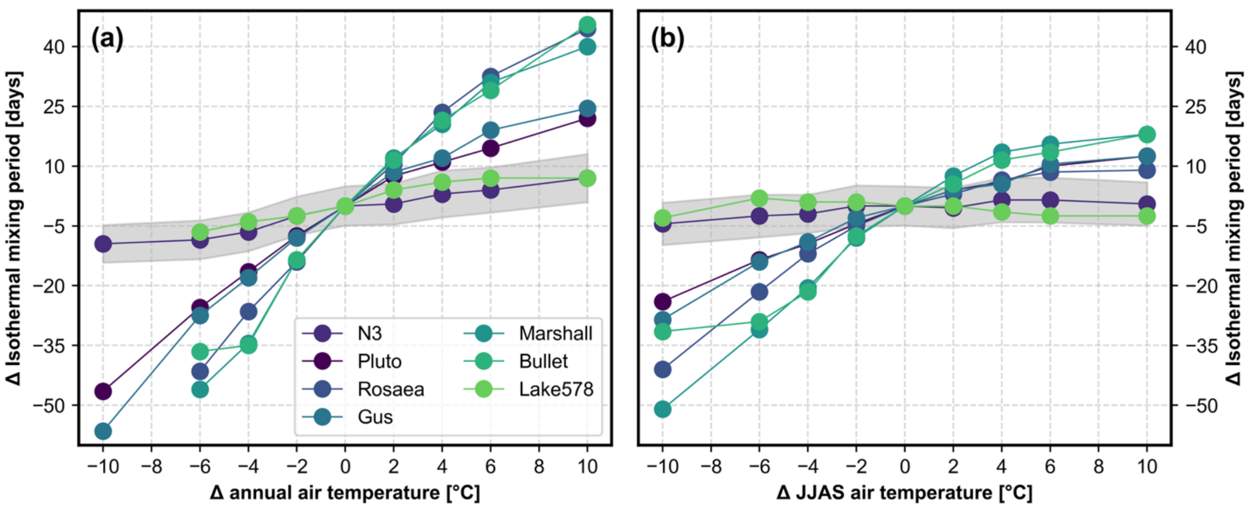

Figure S19: Simulation of the isothermal mixing period (days, defined as mixing depth = 75% of maximum lake depth) in studied lakes to changes in (a) annual air temperature and (b) JJAS air temperature, shown as anomalies relative to the simulation under modern climate. Each point denotes the median value of the 30-year simulation. Grey shading represents the standard deviation for the 30 years simulated for Lake N3.

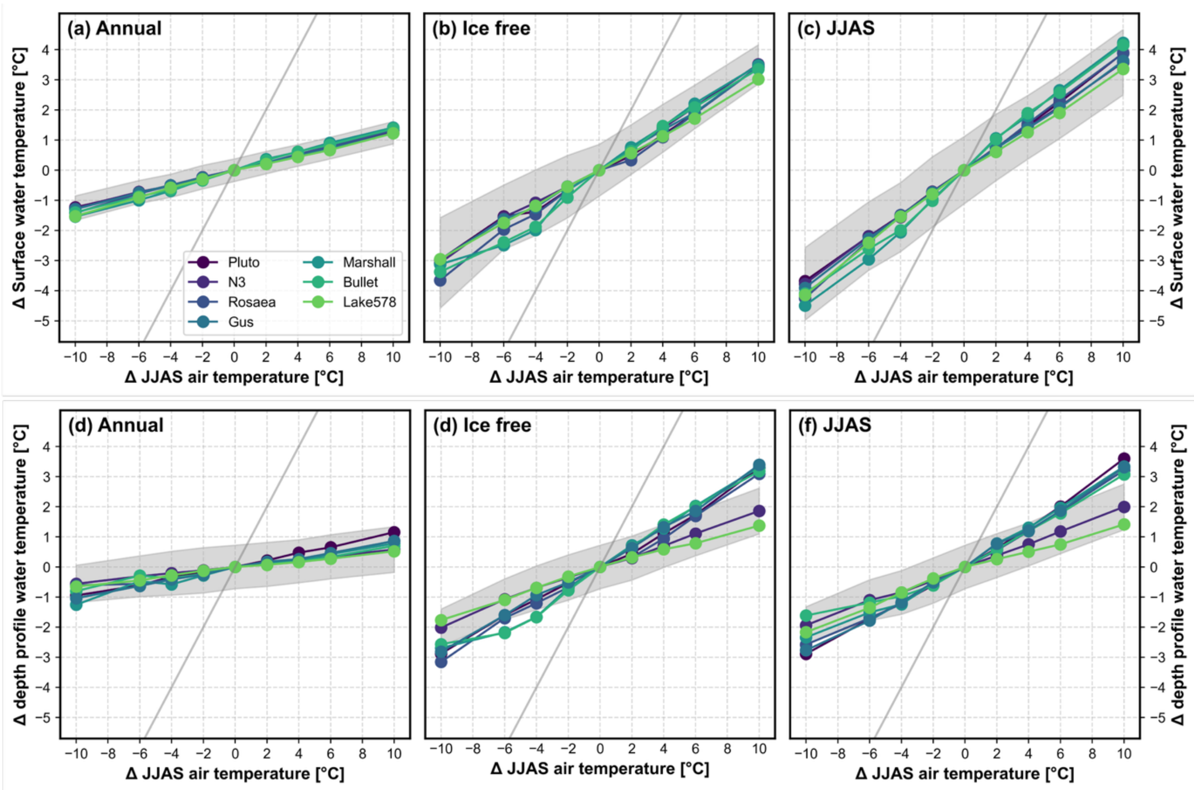

Figure S20: Sensitivity of surface water (a–c) and area-weighted average depth profile temperatures (d–f) to changes in annual air temperature. (a) and (d) annual, (b) and (e) IFS, (c) and (f) JJAS water temperature [°C]. Each point denotes the median value of the 30-year simulation. The grey line is the 1:1 line. Grey shading represents the standard deviation for the 30 years simulated for Lake N3. Standard deviation is on the same order as for other lakes.

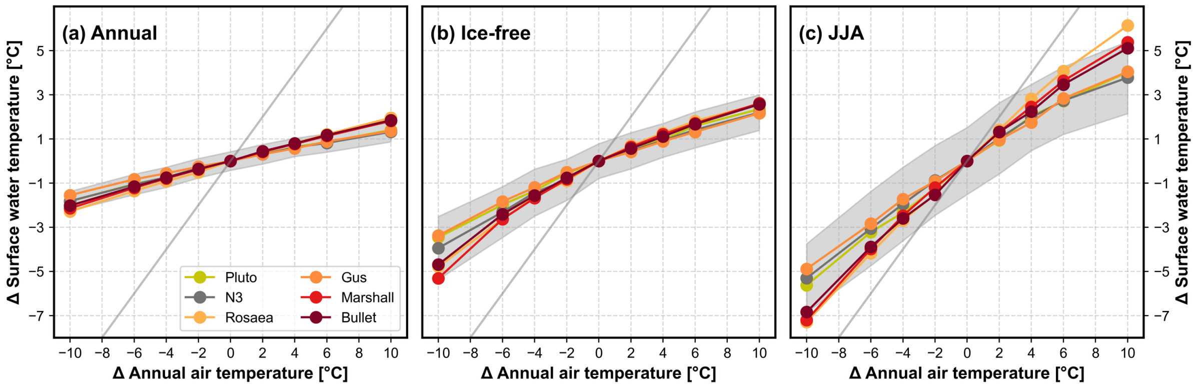

Figure S21: Sensitivity of average surface water temperature to changes in annual air temperature with neutral drag coefficient 1.0e^{-3} and light extinction coefficient 0.1. Changes in (A) annual (B) ice-free and (C) JJA surface water temperature [°C], with changes in annual air temperature.

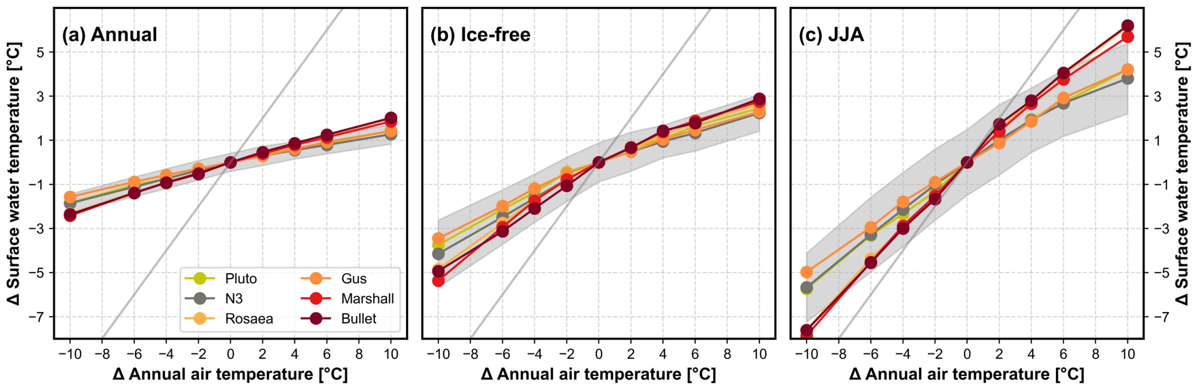

Figure S22: Sensitivity of average surface water temperature to changes in annual air temperature with neutral drag coefficient 1.0e^{-3} and light extinction coefficient 1.0. Changes in (A) annual (B) ice-free and (C) JJA surface water temperature [°C], with changes in annual air temperature.

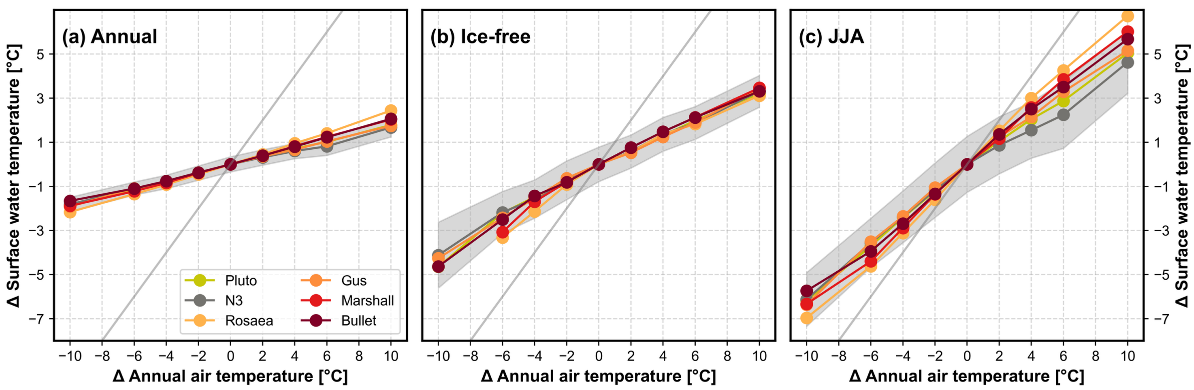

Figure S23: Sensitivity of average surface water temperature to changes in JJAS air temperature with neutral drag coefficient = 2.5e^{-3} and light extinction coefficient = 0.1. Changes in (A) annual (B) ice-free and (C) JJA surface water temperature [°C], with changes in annual air temperature.

Supplementary tables:

Table S1. The ^{14}C calculation parameters, radiocarbon ages and 2σ calibrated ages for the sediment core from Lake Marshall. All ^{14}C-ages were calibrated using IntCal20 calibration dataset (Reimer et al., 2020).

Accession #	**Core**	**Top depth (cm)**	**Sample thickness (cm)**	**Sample material**	**$F^{14}C$ modern**	**Fm err**	**$\delta^{13}C$ (‰)**	**^{14}Cage and uncertainty (yr)**	**Median calibrated age (yr BP) and 2σ uncertainty (yr)**
OS-138405	17MAR-C1	7	1	Aquatic macrofossils	0.8049	0.0017	-24.34	495 ± 20	523 ± 17
OS-144352	17MAR-C1	16.5	0.5	Aquatic macrofossils	0.8804	0.0019	-22.48	1020 ± 20	936 ± 21
OS-144353	17MAR-C1	48	1	Aquatic macrofossils	0.6541	0.0016	-25.93	3410 ± 20	3648 ± 119
OS-151282	17MAR-C1	60	1.5	Aquatic macrofossils	0.6321	0.0017	-28.72	3680 ± 20	4035 ± 81
OS-151378	17MAR-C1	73	1.5	Aquatic macrofossils	0.5229	0.0018	-27.81	5210 ± 30	5966 ± 126
OS-144354	17MAR-C1	83.5	0.5	Aquatic macrofossils	0.4550	0.0018	-27.37	6330 ± 30	7251 ± 76
OS-137548	17MAR-C1	104.5	0.5	Aquatic macrofossils	0.37700	0.007	-27.3	8690 ± 330	9763 ± 932

Table S2. The ^{14}C calculation parameters, radiocarbon ages, and 2σ calibrated ages for the sediment core from Bullet Lake.

Accession #	Core	Top depth (cm)	Sample thickness (cm)	Sample material	$F^{14}C$ modern	Fm err	$\delta^{13}C$ (‰)	^{14}Cage and uncertainty (yr)	Median calibrated age (yr BP) and 2σ uncertainty (yr)
OS-144491	17BLT-A1a	5.25	0.5	Aquatic macrofossils	1.0061	0.0024	-23.92	-5 ± 1	-5 ± 1*
OS-151280	17BLT-A1a	20	0.5	Aquatic macrofossils	0.8383	0.0019	-25.74	1420 ± 20	1324 ± 26
OS-144350	17BLT-A1a	48.5	0.5	Aquatic macrofossils	0.7691	0.0020	-26.68	2110 ± 20	2071 ± 72
OS-151376	17BLT-A1b	75	0.5	Aquatic macrofossils	0.6450	0.0021	-28.61	3520 ± 25	3781 ± 90
OS-144351	17BLT-A1b	87	4	Aquatic macrofossils	0.6064	0.0021	-29	4020 ± 30	4479 ± 77
OS-151281	17BLT-A1b	111	0.5	Aquatic macrofossils	0.4969	0.0017	-29.23	5620 ± 20	6393 ± 87
OS-151370	17BLT-A1b	119	0.5	Aquatic macrofossils	0.4802	0.0081	-25.72	5890 ± 140	6715 ± 381
OS-144131	17BLT-A1b	126	0.7	Aquatic macrofossils	0.4212	0.0017	-26.73	6950 ± 30	7773 ± 114
OS-151377	17BLT-A1b	140.5	0.5	Aquatic macrofossils	0.4117	0.0041	-25.4	7130 ± 80	7949 ± 193

*Indicates a ^{14}C-age calibrated with the bomb peak Northern Hemisphere 1 calibration dataset (Hua et al., 2013). The rest of the ^{14}C-ages were calibrated using IntCal20 calibration dataset (Reimer et al., 2020).

Table S3. The ^{14}C calculation parameters, radiocarbon ages, and 2σ calibrated ages for the sediment core from Rosaea Lake. All ^{14}C-ages were calibrated using IntCal20 calibration dataset (Reimer et al., 2020).

LabID	Core	Top depth (cm)	Sample thickness (cm)	Sample material	$F^{14}C$ modern	Fm err	$\delta^{13}C$ (‰)	^{14}C-age and uncertainty (year)	Median calibrated age (yr BP) and 2σ uncertainty
OS-147583	18ROS-A2a	4	0.5	Aquatic macrofossils	0.9097	0.0020	-28.0	760 ± 20	683 ± 20
OS-147584	18ROS-A2a	30	0.5	Aquatic macrofossils	0.8321	0.0017	-24.79	1480 ± 15	1359 ± 20
OS-151277	18ROS-A2a	62	0.5	Aquatic macrofossils	0.7525	0.0019	-28.22	2280 ± 20	2321 ± 20
OS-151278	18ROS-A2a	89.5	0.5	Aquatic macrofossils	0.6843	0.0016	-27.29	3050 ± 20	3264 ± 20
OS-151279	18ROS-A2b	124	0.5	Aquatic macrofossils	0.6009	0.0016	-24.5	4090 ± 20	4579 ± 20
OS-147585	18ROS-A2b	124	0.5	Aquatic macrofossils	0.5955	0.0015	-28.34	4160 ± 20	4706 ± 20
OS-151375	18ROS-A2b	166.5	0.5	Aquatic macrofossils	0.5158	0.0018	-26.9	5320 ± 30	6089 ± 20
OS-151136	18ROS-A2b	172.5	0.5	Aquatic macrofossils	0.5041	0.0017	-25.83	5500 ± 30	6297 ± 20
OS-144356	18ROS-A2b	237.5	0.5	Aquatic macrofossils	0.3551	0.0019	-23.44	8320 ± 45	9342 ± 20

Table S4: Correlation (r-value and p-value) between the ratio of caldarchaeol to crenarchaeol (Cald/Cren) and reconstructed temperature. Significant correlations ($p < 0.05$) are bolded.

Lake	Cald/Cren vs. Temperature	Cald/Cren vs HP5	Cald/Cren vs %IIIa	HP5 vs Temperature	%IIIa vs Temperaure
Pluto	**-0.58 (p<0.01)**	**0.64 (p<0.01)**	-0.19 (p=0.38)	**-0.79 (p<0.01)**	**-0.73 (p<0.01)**
N3	0.04 (p=0.74)	-0.22 (p=0.07)	**-0.45 (p<0.01)**	**-0.49 (p<0.01)**	**-0.61 (p<0.01)**
Rosaea	**-0.55 (p<0.01)**	**0.42 (p<0.01)**	**0.51 (p<0.01)**	**-0.84 (p<0.01)**	**-0.95 (p<0.01)**
Marshall	-0.40 (p=0.07)	**0.43 (p=0.05)**	0.31 (p=0.16)	**-0.90 (p<0.01)**	**-0.91 (p<0.01)**
Bullet	**-0.70 (p<0.01)**	0.16 (p=0.47)	-0.30 (p=0.18)	**-0.56 (p<0.01)**	**-0.63 (p<0.01)**
Gus	**0.64 (p<0.01)**	**-0.80 (p<0.01)**	**-0.92 (p<0.01)**	**-0.61 (p<0.01)**	**-0.83 (p<0.01)**
578	**-0.45 (p<0.01)**	**0.26 (p=0.01)**	**0.06 (p=0.52)**	**-0.65 (p<0.01)**	**-0.68 (p<0.01)**

References

Blaauw, M., & Christen, J. A. (2011). Flexible paleoclimate age-depth models using an autoregressive gamma process. *Bayesian Analysis*, *6*(3), 457–474. https://doi.org/10.1214/11-BA618

Corcoran, M. C., Thomas, E. K., & Morrill, C. (2021). Using a Paired Chironomid δ^{18}O and Aquatic Leaf Wax δ^{2}H Approach to Reconstruct Seasonality on Western Greenland During the Holocene. *Paleoceanography and Paleoclimatology*, *36*(4), e2020PA004169. https://doi.org/10.1029/2020PA004169

Hua, Q., Barbetti, M., & Rakowski, A. Z. (2013). Atmospheric Radiocarbon for the Period 1950–2010. *Radiocarbon*, *55*(4), 2059–2072. https://doi.org/10.2458/azu_js_rc.v55i2.16177

McKay, N. P., Emile-Geay, J., & Khider, D. (2021). geoChronR – an R package to model, analyze, and visualize age-uncertain data. *Geochronology*, *3*(1), 149–169. https://doi.org/10.5194/gchron-3-149-2021

Raberg, J. H., Harning, D. J., Crump, S. E., de Wet, G., Blumm, A., Kopf, S., et al. (2021). Revised fractional abundances and warm-season temperatures substantially improve brGDGT calibrations in lake sediments. *Biogeosciences*, *18*(12), 3579–3603. https://doi.org/10.5194/bg-18-3579-2021

Reimer, P. J., Austin, W. E. N., Bard, E., Bayliss, A., Blackwell, P. G., Bronk Ramsey, C., et al. (2020). The IntCal20 Northern Hemisphere Radiocarbon Age Calibration Curve (0–55 cal kBP). *Radiocarbon*, *62*(4), 725–757. https://doi.org/10.1017/rdc.2020.41

Thomas, E. K., Briner, J. P., Ryan-Henry, J. J., & Huang, Y. (2016). A major increase in winter snowfall during the middle Holocene on western Greenland caused by reduced sea ice in Baffin Bay and the Labrador Sea. *Geophysical Research Letters*, *43*(10), 5302–5308. https://doi.org/10.1002/2016GL068513

Thomas, E. K., Hollister, K. V., Cluett, A. A., & Corcoran, M. C. (2020). Reconstructing Arctic Precipitation Seasonality Using Aquatic Leaf Wax δ ^{2} H in Lakes With Contrasting Residence Times. *Paleoceanography and Paleoclimatology*, *35*(7), e2020PA003886. https://doi.org/10.1029/2020PA003886

Weber, Y., De Jonge, C., Rijpstra, W. I. C., Hopmans, E. C., Stadnitskaia, A., Schubert, C. J., et al. (2015). Identification and carbon isotope composition of a novel branched GDGT isomer in lake sediments: Evidence for lacustrine branched GDGT production. *Geochimica et Cosmochimica Acta*, *154*, 118–129. https://doi.org/10.1016/j.gca.2015.01.032

Zhao, B., Castañeda, I. S., Bradley, R. S., Salacup, J. M., De Wet, G. A., Daniels, W. C., & Schneider, T. (2021). Development of an in situ branched GDGT calibration in Lake 578, southern Greenland. *Organic Geochemistry*, *152*, 104168. https://doi.org/10.1016/j.orggeochem.2020.104168